Available online at www.sciencedirect.com

ScienceDirect

Procedia Engineering 99 (2015) 384 – 390

Procedia Engineering

www.elsevier.com/locate/procedia

"APISAT2014", 2014 Asia-Pacific International Symposium on Aerospace Technology, APISAT2014

Investigation of Airfoil Unsteady Aerodynamic Characteristics Based on Finite Macro-Element and TFI Hybrid Dynamic Mesh Correction

TANG Han, GAO Zhenxun*

National Laboratory of Computatioal Fluid Dynamics, Beihang University, Beijing 100191, China

Abstract

The hybrid dynamic mesh method combining finite macro-element with transfinite interpolation (TFI) is adopted in this paper which ensures mesh quality for large deformations and high efficiency. Besides, TFI is modified to preserve the grid orthogonality near the boundary using rotation correction and weighted approach in order to solve its orthogonal problem. The numerical simulation of oscillating airfoil is performed by solving Reynolds Averaged Navier-Stokes (RANS) equations with hybrid dynamic mesh method. The influences of oscillation parameters and Mach number on the hysteresis effect are investigated and the separation vortex pattern and evolution procedure are presented. Moreover, numerical results show the occurrence of lock-in zone. The effect of oscillation amplitude and frequency on it and the characteristics of vortex shedding are discussed.

Peer-review under responsibility of Chinese Society of Aeronautics and Astronautics (CSAA)

Keywords: finite macro-element; TFI; hysteresis effect; vortex shedding; lock-in

1. Introduction

Research on unsteady dynamic numerical simulation of airfoil is significant for airfoil aerodynamic characteristics and flow mechanism. However, there are still some problems in the present work. First, it is necessary

* Corresponding author. Tel.: +86 10 82315396; fax: +86 10 82315396.
E-mail address: gaozhenxun@163.com

Peer-review under responsibility of Chinese Society of Aeronautics and Astronautics (CSAA)
doi:10.1016/j.proeng.2014.12.551

to use dynamic mesh to deform the flow field mesh in unsteady numerical simulation with moving boundary. Excellent dynamic mesh deformation capacity is crucial. Second, unsteady flow mechanism is not still deeply understood such as hysteresis effect and lock-in which need further investigation.

The transfinite interpolation (TFI) [1] and finite macro-element [2] are two popular structured dynamic mesh deformation techniques. The former has higher efficiency but worse orthogonality for large deformations. The latter can deform in a large range, but increases workload and has lower efficiency. Therefore, the research of hybrid dynamic mesh method which combines finite macro-element and TFI is worthwhile.

There are plenty of experimental and numerical researches [3-4] on the hysteresis, dynamic stall problems at home and abroad which focus on turbulence models and the effect of parameters. There are studies [5-7] on the lock-in and phase shift between unsteady force and movement displacements in oscillating cylinder flows, but the numerical investigations of the vortex shedding formation and unsteady force on oscillating airfoil are still very few. Due to the complexity of the problems, unsteady flow mechanism of oscillating airfoil needs to be studied deeply.

The hybrid dynamic mesh method combining finite macro-element and TFI is developed which is improved by rotation correction. The numerical simulations of unstalled and dynamic stalled problems for oscillating airfoil are carried out by solving Reynolds Averaged Navier-Stokes (RANS) equations. The relationship between oscillating frequency and vortex shedding frequency is also investigated, which is valuable in engineering application.

2. Numerical method

2.1. Navier-Stokes equations for dynamic grids

The time-dependent Reynolds-averaged Navier-Stokes equations for dynamic grids can be written in the integral form as following:

$$\frac{\partial}{\partial t}\int_V \mathbf{Q}\,\mathrm{d}V + \oint_S (\mathbf{F}^{\mathbf{i}}(\mathbf{Q}) - \mathbf{Q}\mathbf{v}_{\mathbf{g}} \bullet \mathbf{n})\,\mathrm{d}S = \oint_S \mathbf{F}_{\mathbf{v}}\,\mathrm{d}S \tag{1}$$

where S is the surface surrounding the control volume V, $\mathbf{n}$ is the outgoing unit normal of S, $\mathbf{v_g}$ is the velocity of S, $\mathbf{Q}$ is the vector of conservative variables, $\mathbf{F^i}$ is the inviscid and $\mathbf{F_v}$ the viscous flux vectors.

2.2. Numerical discretization

The Roe scheme with second-order accuracy and the second-order center difference scheme are used for inviscid flux and viscid flux discretization respectively. In addition, Dual-time step is adopted and the acceleration convergence methods such as local time step and multigrid are also utilized in pseudo time step.

To avoid the numerical errors caused by grid deformation, the geometric conservation law (GCL) needs to be satisfied.

In the far field, a characteristic analysis based on Riemann invariants is used to determine the values of the flow variables. For an unsteady viscous surface boundary, no-slip boundary condition is used. The velocity components at the ghost cell are computed as: $u_{ghost} = -u + 2n_xV_t$, $v_{ghost} = -v + 2n_yV_t$, $V_t = \mathbf{V_g} \bullet \boldsymbol{n}$.

2.3. Dynamic mesh deforming strategy

Structured multi-block deformation is performed in two steps. First of all, each block of the computation domain is divided into several sub-blocks by the element node (or control points). The block corner displacement is finite element solution of macro-element points computed by solving elastic solid deformation equations. The resulting solution transmits boundary movement to the element nodes. Next, the interior grid displacement is obtained by interpolating the corner displacement using TFI blending function.

The constitutive relationships between stresses and strains are given by Hooke's law for a macro-element m.

$$\boldsymbol{\sigma}_{\mathbf{m}} = \mathbf{C}_{\mathbf{m}}\boldsymbol{\varepsilon}_{\mathbf{m}} \tag{2}$$

where

$$\boldsymbol{\sigma}_m = \begin{bmatrix} \sigma_{xx} \\ \sigma_{yy} \\ \sigma_{zz} \\ \sigma_{xy} \\ \sigma_{yz} \\ \sigma_{xz} \end{bmatrix}, \quad \boldsymbol{\varepsilon}_m = \begin{bmatrix} \varepsilon_{xx} \\ \varepsilon_{yy} \\ \varepsilon_{zz} \\ \varepsilon_{xy} \\ \varepsilon_{yz} \\ \varepsilon_{xz} \end{bmatrix}, \quad \boldsymbol{C}_m = \begin{bmatrix} E_m & 0 & 0 & 0 & 0 & 0 \\ 0 & E_m & 0 & 0 & 0 & 0 \\ 0 & 0 & E_m & 0 & 0 & 0 \\ 0 & 0 & 0 & G_m & 0 & 0 \\ 0 & 0 & 0 & 0 & G_m & 0 \\ 0 & 0 & 0 & 0 & 0 & G_m \end{bmatrix} \tag{3}$$

$$E_m = E_0 f_m, \; G_m = G_0 f_m, \; f_m = \frac{1}{1-e^{(-\beta_1 \Delta r_m / \Delta r_{\max})}}, \; \Delta r_m = \sqrt{(\Delta x_{cs,m})^2 + (\Delta y_{cs,m})^2 + (\Delta z_{cs,m})^2} \tag{4}$$

with C_m representing elastic matrix and E_m and G_m representing Young's shearing modulus. The subscript $(\,)_c$ and $(\,)_s$ denote the center of element m and boundary point which has minimum distance from the element m. The choice of the function f_m in equation (4) for the moduli decay is determined by the fact that it has the following properties: as Δr_m tends to zero, f_m tends to infinite; Δr_m tends to infinite, f_m tends to one. Macro-element moduli decay exponentially according to the distance from the boundary resulting in large moduli and extremely stiff elements near the moving boundary.

TFI does not take the rotational displacement into account, so it can not maintain the orthogonality near the boundary. The basic procedure of rotation correction is shown below. Firstly, the boundary movements are classified as translation and rotation; Secondly, the rotational vector is introduced, every point rotates around the corresponding boundary point, and then the reference moving grid is attained. Finally, the final grid is achieved by adopting the weighted factor between the initial grid and reference moving grid.

The current grid deforming algorithm is illustrated in Fig. 1. Given a starting grid and a surface displacement, the translation and rotation of each surface node are computed from the deflected aerodynamic surface. Let $\mathbf{X}$ and $\Delta\mathbf{X}$ be the position vector and displacement vector respectively. The translational displacements are: $\Delta\mathbf{X}_i = \mathbf{X}'_{i,1} - \mathbf{X}_{i,1}$.

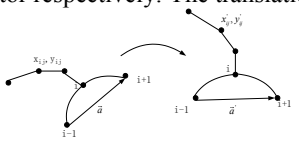

Fig.1. Grid rotation

The rotational displacement can be expressed as

$$\cos\theta_i = \frac{\mathbf{a} \bullet \mathbf{a}'}{|\mathbf{a}||\mathbf{a}'|}, \quad \sin\theta_i = \frac{(\mathbf{a} \times \mathbf{a}') \bullet \mathbf{e}_z}{|\mathbf{a}||\mathbf{a}'|} \tag{5}$$

where $\mathbf{a}$ is the original surface vector from i - 1 to i + 1 and $\mathbf{a}'$ is surface vector in next time step. Each grid (i, j) is then moved in a rigid body way according to the displacement of the surface node to form a reference. The reference moving grid position is defined by $\mathbf{X}^{\text{ref}}_{i,j} = \mathbf{M}_{\text{rot}}(\mathbf{X}_{i,j} - \mathbf{X}_{i,1}) + \mathbf{X}_{i,1} + \Delta\mathbf{X}_i$, where $\mathbf{M}_{\text{rot}}$ is the rotational transformation matrix and can be expressed as:

$$\mathbf{M}_{\text{rot}} = \begin{bmatrix} \cos\theta & -\sin\theta \\ \sin\theta & \cos\theta \end{bmatrix} \tag{6}$$

Weights the positions of initial grid and reference grid, then the new position in next time step is obtained. $\mathbf{X}'_{i,j} = \omega_{i,j}\mathbf{X}_{i,j} + (1-\omega_{i,j})\mathbf{X}^{\text{ref}}_{i,j}$.

Choosing the weighted factor ω properly, the mesh quality near the boundary is maintained. Let j be the normal

index, the weighed factor can be expressed as: $\omega = \omega(j) = 3\chi^2 - 2\chi^3$ where $\chi = ((j - 1)/(j_{max} - 1))^{\gamma}$ and γ is constant chosen experientially.

3. Results and discussions

3.1. The hybrid dynamic mesh based on finite macro-element and TFI

The grid used here for computations is a C-type grid consisting of 385x65 mesh cells. The average spacing for the first layer of points from the airfoil surface is approximately $1x10^{-6}$. The airfoil oscillates about its quarter chord. Figures 2(a)-(b) show the original user-defined macro-elements and mesh. Figures 2(c)-(d) present the final macro-element and mesh after the airfoil is pitched to 45°. It is shown the grid orthogonality near the boundary is very good.

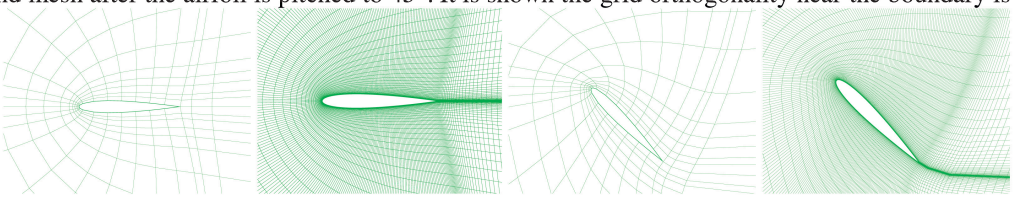

Fig. 2. (a) User defined macro-elements; (b) Initial mesh; (c) Final Macro-elements; (d) Final mesh

The orthogonality is ensured by large stiffness near the boundary which mainly relies on the distribution of control points and choosing control points improperly may lead to negative volume. To consider the effect of rotation correction, Figures 3 and 4 give the result of airfoil pitched to 60° using TFI and modified method respectively. It is shown that the orthogonality is bad near the boundary using TFI in Fig. 3. However, the mesh quality is very good using modified TFI when the airfoil rotates 60° as Fig. 4 shown.

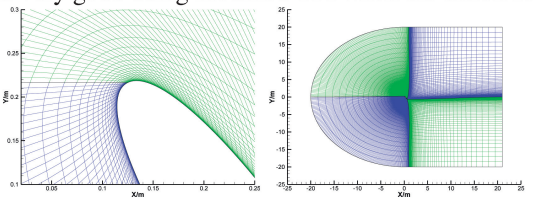

Fig. 3. (a) Local view; (b) Global view

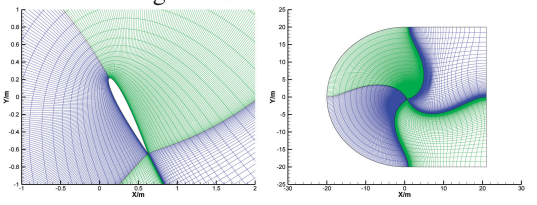

Fig. 4. (a) Local view; (b) Global view

3.2. Unstalled airfoil flow

The harmonic pitching motion about the quarter chord is defined as $\alpha(t) = \alpha_m + \alpha_0 \sin(2kt)$, Where α_m is the mean angle of attack, and α_0 the amplitude of the oscillation. The oscillation frequency, which is an important similarity parameter for this unsteady problem, is defined as $f = \omega c/2V_\infty$ where V_∞ is the free-stream velocity and c the chord length of the airfoil. The computational condition is : $M_\infty = 0.755$, $\alpha_m = 0.016°$, $\alpha_0 = 2.51°$ and $k = 0.0814$.

The unsteady calculation was started from a steady-state solution of the mean angle of attack. Figure 5 shows the plots of lift and moment coefficients vs. angle of attack respectively. The changes of lift and moment coefficients vs. angle of attack are lagged which show hysteresis effect of unsteady flows. Also shown is a comparison with the experimental data of Landon [3]. The present computational results agree very well with experiments.

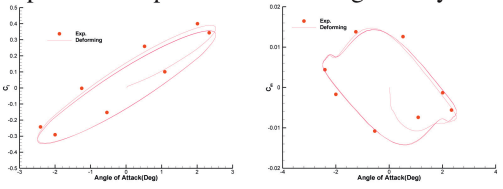

Fig. 5. (a) Lift coefficient vs. angle of attack; (b) Moment coefficient vs. angle of attack

Figure 6(a) gives the hysteresis curve of the moment coefficient for different amplitude 1.5°, 2.51° and 3.50° at the same oscillation frequency. Also, hysteresis curve of the moment coefficient is displayed in Fig. 6(b) for different oscillation frequency 0.1628, 0.0814, 0.0412 at the same amplitude. It is shown that the hysteresis effect increases with the increase of oscillation amplitude and frequency. The hysteresis curve of the moment coefficient for different Mach number is also shown in Fig. 6(c). It can be seen that the hysteresis loop grows larger at first and then become smaller with the increase of Mach number.

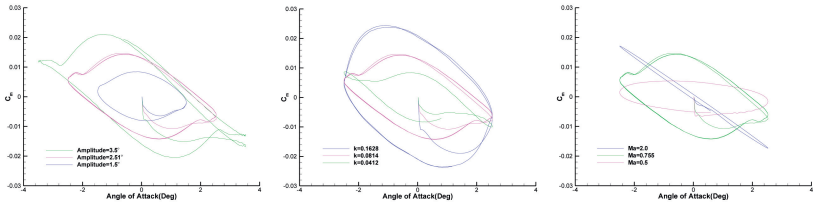

Fig. 6. (a) For different amplitude; (b) For different oscillation frequency; (c) For different Mach number

3.3. Dynamic stall simulation

The dynamic stall problem in Ref. [4] is chosen for test case for validation. Figure 7 displays the plots of lift and moment coefficients vs. angle of attack with different turbulence models. The result shows that the k-ω SST turbulence model can simulate the hysteresis loop of aerodynamic coefficient more accurately and the hysteresis loop of aerodynamic coefficient predicted by this model is in agreement with the experiment data.

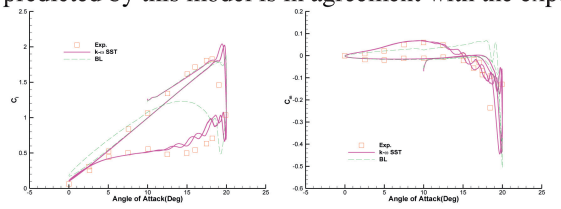

Fig. 7. (a) Lift coefficient loop; (b) Moment coefficient loop

In order to analyze the stall mechanism, the following flow parameters are chosen: $M_\infty = 0.3$, $Re = 7.7 \times 10^4$, $\alpha_m = 10°$, $\alpha_0 = 10°$ and $k = 0.0396$. By analyze the instantaneous streamline contour, the vortex structure and evolvement procedure with the variation of the angle of attack are as follows: When airfoil moves upward, leading edge separation vortex is formed at first with large influence region. When the large separation vortex move downstream which leads to a decrease in lift coefficient. When the airfoil moves downward, the induced second vortex occurs in trailing edge as shown in Fig. 8(b). The trailing edge vortex grows larger and extends upward which raises the position of separation vortex. The raised separation vortex is squeezed by trailing edge vortex and splits into two parts: the one is shed downstream and the other lies on the airfoil surface and becomes larger as Figs. 8(b)-(c) shown making the trailing edge vortex escape from the airfoil as Figs. 8(c)-(e) shown. With the downward movement of the airfoil, the flow becomes attached. It is evident that the vortex formation and size in Fig. 8(e) is very similar to that in Fig. 8(a) which constructs a period. It can be revealed from instantaneous streamlines that the high frequency oscillations in the lift coefficient curve are due to the physics of trailing edge vortex shedding.

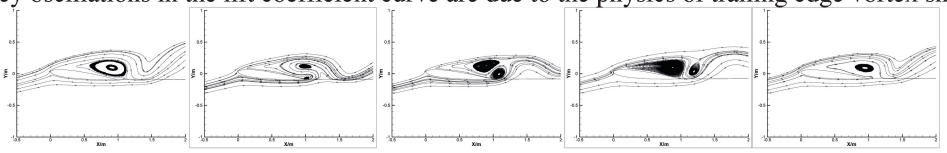

Fig. 8. (a) t = 29.4; (b) t = 29.9; (c) t = 30.5; (d) t = 31.0; (e) t = 31.6

3.4. Oscillation frequency and vortex shedding frequency

When the vortex shedding frequency is synchronized with the oscillation frequency, then lock-in occurs. The vortex shedding pattern and lock-in characteristics are investigated numerically in this paper. The computational condition is : $M_\infty = 0.3$, $Re = 7.7 \times 10^4$, $\alpha_m = 20°$ and $\alpha_0 = 5°$.

As shown in Fig. 9, for $St/St_s = 0.95$, the vortex-shedding frequency f_v is no longer equal to the vortex shedding frequency f_s for the stationary airfoil. Vortices are shed at the oscillation frequency f. This means that the oscillating airfoil and the vortex shedding have the same characteristic frequency. The lock-in has taken place. The occurrence of the lock-in results in one dominant component in the lift coefficient curves. The lift acting on the airfoil is in phase with the airfoil oscillation. In the lock-in zone, the phase difference between the lift coefficient C_l and the airfoil's oscillation displacement is evaluated. A sine wave which has the same period and phase with angular displacement is also given in Fig. 9 for comparison. It can be seen that the amplitude of aerodynamic coefficient becomes larger evidently than that in Fig. 10 and the phase shift is approximately 90° in lock-in zone.

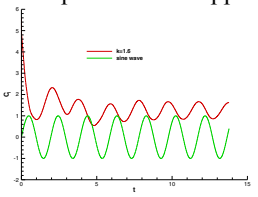

Fig. 9 $St/St_s = 0.95$

As shown in Fig. 10, vortices are shed at a frequency fv that is approximately equal to the vortex shedding frequency fs of the static airfoil but different from the forcing frequency f of the airfoil oscillation. In addition to the strong vibration corresponding to the forced oscillation, periodic fluctuations occur in the time history of the calculated lift coefficient shown in Fig. 10 for St/Sts = 0.095, 0.047, 0.0235. These periodic fluctuation frequencies correspond to the vortex-shedding frequencies. This means that the vortex-shedding frequency is different from the forced oscillation frequency and the flow is not synchronized. In addition, it can be seen from Fig. 11 that there is also hysteresis loop of vortex shedding frequency in which the vortex shedding frequency is lower in downward phase than that in upward phase.

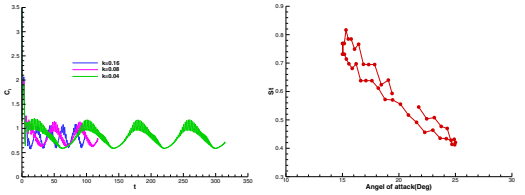

Fig. 10 $St/St_s = 0.095, 0.047, 0.0235$ Fig. 11 Vortex shedding hysteresis curve

The onset of vortex lock-in due to the external forced oscillation determined by the combination of the forced oscillation frequency and amplitude. The calculations for different forcing frequencies and angular displacement amplitudes are carried out. For different angular displacement amplitudes 0.001°and 5° at fixed St/Sts = 0.9, lock-in occurs for amplitude 5°. However, when the amplitude is decreased to 0.001°, vortices are shed at natural vortex shedding frequency. It is found that lock-in occurs when the amplitude is greater than a threshold value. For different St/Sts = 0.68, 0.8 and 0.9, lock-in takes place at St/Sts = 0.8 and 0.9, amplitude 5°, but no lock-in takes place at amplitude 3°. The forcing amplitude for the onset of lock-in increases with an increase in the difference between the forcing and natural shedding frequencies.

4. Inclusions

In this paper, dynamic mesh technology and unsteady aerodynamic characteristics are investigated, some

conclusions can be drawn:

The hybrid dynamic mesh method combining finite macro-element and TFI can maintain mesh quality in large deformation. The rotation correction of TFI can preserve the orthogonality near the boundary when airfoil rotates 60°.

For the unstalled problem, it is found that the hysteresis effect strengthens with the increase of oscillation amplitude and frequency and the hysteresis loop grows larger at first and then become smaller with the increase of Mach number. For the dynamic stall problem, the k-ω SST turbulence model is effective to simulate the dynamic stall. The separation vortex formation, development and vortex shedding are analyzed in detail.

The relation of oscillation frequency and vortex shedding frequency is also investigated. When oscillation frequency is small, the vortex shedding relates to the natural shedding frequency of corresponding angle of attack and there is hysteresis loop of vortex shedding frequency in which the vortex shedding frequency is lower in downward phase than that in upward phase. When the oscillation frequency increases by nearing the natural shedding frequency of mean attack angle, the vortex shedding frequency is synchronized with the oscillation frequency, thus lock-in occurs. During lock-in regime, vortices are forcibly shed at the vibration frequency, rather than at the Strouhal frequency. In the lock-in zone, the amplitude of aerodynamic coefficients increases greatly and phase shift is approximately 90°. Furthermore, the onset of vortex-shedding lock-in depends on the combination of the forced oscillation frequency and amplitude. The results show that lock-in occurs only above a threshold amplitude of oscillation and the lock-in range increases with increasing amplitude.

References

[1] Gaitonde A L, Fiddes S P. A moving mesh system for the calculation of unsteady flows[R]. AIAA 1993-0641, 1993.

[2] Tezduyar T E. Stabilized finite element formulations for incompressible flow computations[J]. Advances in Applied Mechanics, 1992, 28(1):1-44.

[3] Landon H. Compendium of unsteady aerodynamic measurements[R]. AGARD Report No. 702, 1983

[4] Dindar M, Kaynak U. Effect of turbulence modeling on dynamic stall of a NACA0012 airfoil[R]. AIAA 1994-0190, 1994

[5] Karniadakis, G. E., and Triantafyllou, G. S., “Frequency Selection and Asymptotic States in Laminar Wakes,” Journal of Fluid Mechanics, Vol. 199, Feb. 1989, pp. 441–469.

[6] Koopman, G. H., “The Vortex Wakes of Vibrating Cylinders at Low Reynolds Numbers,” Journal of Fluid Mechanics, Vol. 28, May 1967, pp. 501–512.

[7] Patnaik, B. S. V., Narayana, P. A. A., and Seetharamu, K. N.,“Numerical Simulation of Laminar Flow Past a Transversely Vibrating Circular Cylinder,” Journal of Sound and Vibration, Vol. 228, No. 3,1999, pp. 459–475.